

Simulations of stellar/pulsar-wind interaction along one full orbit

V. Bosch-Ramon¹, M.V. Barkov^{2,3}, D. Khangulyan⁴, and M. Perucho⁵

¹ Dublin Institute for Advanced Studies, 31 Fitzwilliam Place, Dublin 2, Ireland; valenti@cp.dias.ie

² Max Planck Institut für Kernphysik, Saupfercheckweg 1, Heidelberg 69117, Germany

³ Space Research Institute, 84/32 Profsoyuznaya Street, Moscow, Russia

⁴ Institute of Space and Astronautical Science/JAXA, 3-1-1 Yoshinodai, Chuo-ku, Sagamihara, Kanagawa 252-5210, Japan; khangul@astro.isas.jaxa.jp

⁵ Dept. d'Astronomia i Astrofísica, Universitat de València, C/ Dr. Moliner 50, 46100, Burjassot (València), Spain; Manel.Perucho@uv.es

Received jdatej / Accepted jdatej

ABSTRACT

Context. The winds from a non-accreting pulsar and a massive star in a binary system collide forming a bow-shaped shock structure. The Coriolis force induced by orbital motion deflects the shocked flows, strongly affecting their dynamics.

Aims. We study the evolution of the shocked stellar and pulsar winds on scales in which the orbital motion is important. Potential sites of non-thermal activity are investigated.

Methods. Relativistic hydrodynamical simulations in two dimensions, performed with the code *PLUTO* and using the adaptive mesh refinement technique, are used to model interacting stellar and pulsar winds on scales ~ 80 times the distance between the stars. The hydrodynamical results suggest the suitable locations of sites for particle acceleration and non-thermal emission.

Results. In addition to the shock formed towards the star, the shocked and unshocked components of the pulsar wind flowing away from the star terminate by means of additional strong shocks produced by the orbital motion. Strong instabilities lead to the development of turbulence and an effective two-wind mixing in both the leading and trailing sides of the interaction structure, which starts to merge with itself after one orbit. The adopted moderate pulsar-wind Lorentz factor already provides a good qualitative description of the phenomena involved in high-mass binaries with pulsars, and can capture important physical effects that would not appear in non-relativistic treatments.

Conclusions. Simulations show that shocks, instabilities, and mass-loading yield efficient mass, momentum, and energy exchanges between the pulsar and the stellar winds. This renders a rapid increase in the entropy of the shocked structure, which will likely be disrupted on scales beyond the simulated ones. Several sites of particle acceleration and low- and high-energy emission can be identified. Doppler boosting will have significant and complex effects on radiation.

Key words. Hydrodynamics – X-rays: binaries – Stars: winds, outflows – Radiation mechanisms: nonthermal – Gamma rays: stars

1. Introduction

The binary system PSR B1259–63/LS2883, consisting of a late O star (Negueruela et al. 2011) and a 47 ms pulsar (Johnston et al. 1992), is a powerful GeV and TeV emitter (e.g. Aharonian et al. 2005; Abdo et al. 2011; Tam et al. 2011). The physical processes behind the gamma-ray emission detected in PSR B1259–63/LS2883 are believed to take place in the region where the stellar and pulsar winds collide, which would also produce X-rays and, once the interacting flows have left the system, radio emission (e.g., Tavani & Arons 1997; Johnston et al. 1999; Dubus 2006; Moldón et al. 2011a). The processes underlying the non-thermal radiation in PSR B1259–63/LS2883 seem to be shocks that take place in the two-wind interaction region and accelerate electrons. These electrons most likely radiate from radio-to-X-rays through synchrotron and at GeV and TeV energies through inverse Compton emission (IC), although some gamma rays may come from IC in the unshocked pulsar wind (e.g., Tavani & Arons 1997; Ball &

Kirk 2000; Khangulyan et al. 2007, 2011, 2012). The details of the dynamics of the interacting flows are still poorly known, which affects the interpretation of the observed variability and spectra not only in PSR B1259–63/LS2883 but also in other gamma-ray emitting binaries that may host a non-accreting pulsar (LS 5039 and LS I +61 303, see discussions in, e.g., Chernyakova et al. 2006; Dubus 2006; Romero et al. 2007; Bosch-Ramon & Khangulyan 2009; Torres 2011; Bednarek 2011; Barkov & Khangulyan 2012; HESS J0632+057, see, e.g., Bongiorno et al. 2011; 1FGL J1018.6–5856, see, e.g., Ackermann et al. 2012; Abramowski et al. 2012).

Hydrodynamical and magnetohydrodynamical, relativistic and non-relativistic simulations of stellar/pulsar-wind interactions have been carried out in the past few years. In Romero et al. (2007) and Okazaki et al. (2011), three-dimensional (3D), non-relativistic hydrodynamical (SPH) simulations were carried out to study, on binary scales but including orbital motion, the stellar/pulsar-wind interaction in LS I +61 303 and PSR B1259–63/LS2883. In Okazaki et al. (2011), the authors explicitly studied the interaction with the equatorial disc present in the lat-

Send offprint requests to: V. Bosch-Ramon, e-mail: valenti@cp.dias.es

ter. Bogovalov et al. (2008, 2012) performed axisymmetric, relativistic, hydrodynamical, and magnetohydrodynamical simulations of the stellar/pulsar-wind interaction, with the symmetry axis joining the two stars. The orbital motion was not accounted for, although the impact of the pulsar wind anisotropy was studied. Therefore, from previous work the flow evolution seems to be well-understood on scales up to a few pulsar/star separation distances (a). One can conclude that the shape of the interaction region depends on the pulsar-to-star wind-momentum rate ratio (η), the shocked pulsar wind reaccelerates when flowing away from the shock facing the star, and the bending of the interaction structure due to orbital motion is expected.

An analytical study of the shocked flow evolution on scales larger than a indicated that Coriolis forces related to the orbital motion could amplify the shocked flow bending, terminating the pulsar wind flowing away from the star with a strong shock, and enhance instabilities and mixing in the flow contact discontinuity (CD) (Bosch-Ramon & Barkov 2011). The basic idea is that under typical η -values, $\sim 0.03 - 0.3$, the kinetic luminosity of the pulsar wind dominates that of the star by a factor $\chi \approx 30(\eta/0.1)(v_w/2 \times 10^8 \text{ cm s}^{-1})^{-1}$, where v_w is the stellar wind velocity. Such a high χ -value, the interaction geometry, and the impact of the Coriolis force will eventually lead to the formation of a partially confined, high entropy flow with a strong pressure gradient outwards. This will lead to isotropization of the flow mass, momentum, and energy fluxes, and to reexpansion, with the consequent loss of structure. In this context, non-relativistic two-dimensional (2D) simulations done by Lamberts et al. (2012) showed that the shocked flow may keep a spiral-like shape up to large distances, although the adopted light-to-dense wind luminosity ratios, $\chi \leq 1.25$, and the non-relativistic nature of the simulations may prevent one from generalizing this conclusion.

To study in detail the pulsar/star wind interaction on scales $\gg a$, plus a pulsar wind velocity $v \rightarrow c$, we performed 2D relativistic hydrodynamical simulations including orbital motion, where the flow is homogeneous and perpendicular to the simulated plane. We adopted $\chi = 30$ and $\eta = 0.3$, the latter resulting in a geometry of the interaction region similar, on spatial scales $\sim a$, to the 3D case for $\eta = 0.1$. For complementarity, we also explored the case with $\chi = 60$ and $\eta = 0.6$. We note that for $\eta < 1$ and distances to the star $r \sim a$, the pulsar wind gets diluted faster than the stellar wind in 3D than 2D. This means that in 3D, the shocked winds flowing away from the system are deflected by the Coriolis force at a shorter distance than obtained in the present calculations. Moreover, instabilities are typically less disruptive in 2D. All this shows that the flows simulated here are likely to be more stable than in 3D simulations, which should be carried out in the near future.

The paper is organised as follows: in Sect. 2 we present simulations of the orbital evolution of the flow structure; in Sect. 3, the impact of the value of the pulsar-wind Lorentz factor is studied, and the consequences of adopting a relativistic or a non-relativistic approach discussed; finally, in Sect. 4 we summarize our work and present a discussion of the implications of our results for the non-thermal processes in high-mass binaries hosting a young pulsar.

2. Numerical simulations

2.1. Numerical set-up

The simulations were implemented in 2D with the *PLUTO* code¹ (Mignone et al. 2007), the piece-parabolic method (PPM) (Colella & Woodward 1984), an HLLC Riemann Solver (Mignone & Bodo 2005), and using AMR² through the *Chombo* code³ (Colella et al. 2009). *PLUTO* is a modular Godunov-type code entirely written in C intended mainly for astrophysical applications and high Mach number flows in multiple spatial dimensions. The simulations were run through the MPI (message passing interface) library in the cluster of Moscow State University *Chebyshev*.

The simulated flows were approximated as an ideal, relativistic adiabatic gas with no magnetic field, one particle species, and a polytropic index of 4/3. The adopted resolution was 96×96 cells and 6 levels of AMR, which gives an effective resolution of 6144×6144 cells. The size of the domain was $x \in [0, 80 a]$ and $y \in [0, 80 a]$.

The stellar and pulsar winds were assumed to be isotropic and moving at a constant speed (see below). We thus assumed that the winds had already been accelerated, and did not consider the several effects affecting the state of the two winds before colliding: the ionization/heating effects of X-rays from the shocked winds on the stellar wind formation region (e.g. Blondin 1994); the pressure of the radiation from either the pulsar or the shocked winds exerted on the stellar-wind (e.g. Gayley et al. 1997)⁴; the effects of gravity on slow and dense material within the binary (e.g. Blondin et al. 1991; Okazaki et al. 2011), which are particularly relevant in Be and/or very close systems; and the impact of the stellar radiation field on the pulsar-wind Lorentz factor through Compton braking (e.g. Ball & Kirk 2000; Khangulyan et al. 2007). We note that, even though all these factors may play a major role in particular sources and should be accounted for in more refined treatments of the problem, they can be considered at this stage higher order effects and have therefore been neglected.

A pulsar-wind Lorentz factor $\Gamma = 2$ was adopted because of resolution limitations. This is smaller than the conventional value $\Gamma \sim 10^4 - 10^6$ (see Khangulyan et al. 2012; Aharonian et al. 2012, and references therein), but high enough to reproduce the wind velocity contrast in the bow-like shock region, where instabilities trigger, and to capture important relativistic effects. Similarities and differences between the Γ -value adopted here, a more realistic one, and the non-relativistic case, are discussed in Sect. 3.

The orbit was assumed to be circular, with a period $T = 3 \times 10^5$ s and radius $a = 3 \times 10^{12}$ cm, and $v_w = 0.01 c$, which is typical for the isotropic/polar wind in massive stars. A slow equatorial wind is not considered here (see otherwise Okazaki et al. 2011; Bosch-Ramon & Barkov 2011). For the given η , Γ , and v_w values, the stellar and pulsar-wind momentum rates, normalized to the stellar mass-loss rate $\dot{M}_{-7} = (\dot{M}/10^{-7} M_\odot \text{ yr}^{-1})$, are $\approx 2 \times 10^{27} \dot{M}_{-7}$ and $6 \times 10^{26} \dot{M}_{-7} \text{ g cm s}^{-2}$, respectively, and the pulsar-wind luminosity $\approx 9 \times 10^{36} \dot{M}_{-7} \text{ erg s}^{-1}$. The numerical solution obtained can be used for other orbits with similar values of

¹ Link <http://plutocode.ph.unito.it/index.html>

² Adaptive mesh refinement technique

³ Link <https://commons.lbl.gov/display/chombo/>

⁴ This effect is expected to be minor due to a star luminosity that is much higher than the spin-down one.

T/a . For high \dot{M} - and small a -values, the shocked stellar wind may be radiative instead of adiabatic, enhancing the growth of the flow instability at the CD (see, e.g., Pittard 2009, for two non-relativistic winds).

At the beginning of the simulation, the unperturbed stellar and pulsar winds occupied the two grid halves, left and right, respectively. Both winds were supersonic, of negligible temperature, and had a cylindrical symmetry around axes perpendicular to the simulation plane and crossing the wind sources. The given values of v_w and Γ , together with \dot{M} and η , determine the wind densities. The star and the pulsar were initially located at $(39.5a, 40a)$ and $(40.5a, 40a)$, respectively, and the orbital motion, occurring in the plane XY , was set counter-clockwise. The simulations included neither the magnetic field nor an anisotropic pulsar wind, since their impact is expected to be small (Bogovalov et al. 2012).

2.2. Results

Figures 1 and 4 show the evolution of the density map of the simulated flows during one orbital period, for $\eta = 0.3$ and 0.6, respectively. Physical times earlier than $< 0.3T$ are not shown since the structure had not yet reached a quasi-steady configuration on the scales of interest. The snapshots are obtained at $t \simeq 0.4T$, $0.7T$, and $0.9T$. For the last snapshot time, the tracer map is also shown in Figs. 2 ($\eta = 0.3$) and 5 ($\eta = 0.6$), indicating how much pulsar (1) and stellar wind material (-1) are present in the computational cells. Finally, Figs. 3 ($\eta = 0.3$) and 6 ($\eta = 0.6$) show a map of the module of the four-velocity spatial component (three-velocity module times the flow Lorentz factor). Arrows and their colours in all figures indicate the direction and module of the four-velocity spatial component, respectively.

The flow behavior in the inner bow-shaped interaction region is very similar to that found in previous simulations (e.g., Bogovalov et al. 2008, 2012). In particular, the re-acceleration of the pulsar wind after the termination shock (Bogovalov et al. 2008) is also present in our calculations despite the adopted small Γ -value. This effect can be noticed in the velocity gradient around the shock apex shown in Figs. 3 and 6, with bulk Lorentz factors increasing from ≈ 1.1 to 1.4 (see also Sect. 3). On larger scales, however, the interaction structure starts to depart strongly from being symmetric with respect to the two-star axis. Several orbital-motion effects are apparent. First, the stellar wind pushes clockwise the leading side of the interaction structure, forming strong shocks in both the unterminated and the already terminated pulsar-wind zones. At the leading edge, and in the unterminated pulsar wind flowing away from the binary, a strong shock is formed at the distance of $r \sim 5a$. On the trailing side, the termination takes place at around $r \sim 10a$. Beyond these points, the shocked pulsar wind is deflected by an angle $\sim \pi/2$, and becomes strongly turbulent and increasingly loaded with stellar wind material. We note that, even for highly eccentric systems (such as PSR B1259–63/LS2883), the obtained solution still provides a qualitative description of the shocked structure. The reason is that the characteristic flow speeds exceed the pulsar orbital velocity by at least one order of magnitude. This implies, on the one hand, that the flow structure will adiabatically adjust to the changing a along the orbit. Moreover, the longer orbital timescale compared to that of the shocked

flows will allow the latter to cover a significant fraction of a spiral turn before a has changed significantly.

Turbulence is triggered by the Kelvin-Helmholtz (KH) instability in different regions of the two-wind shocked structure. In its leading edge, the instability grows at the two-wind CD, as also illustrated in Sect. 3. The instability couples with the perturbations generated at the pulsar-wind termination in the opposite direction to the star. At the trailing side, similar processes take place, although the instability grows substantially further, partially because the flow (re)terminates farther, partially because the flow lines diverge there. Bending will make the flow lines of the two shocked winds converge again, but it takes some time for the effect of the Coriolis force to propagate through the shocked structure and cause this convergence.

The tracer maps in Figs. 2 and 5 indicate that already within the first orbital turn, i.e. on scales $\sim (10 - 100)a$, some amount of stellar wind has penetrated deeply into the shocked pulsar flow. This mass-load slows down the shocked pulsar wind, as shown in Fig. 3, and in general makes the flow motion more chaotic, and rich both in weak shocks and turbulence. As seen in the figures, after one orbit the trailing side of the shocked stellar wind already approaches the leading edge, which has already become turbulent.

3. On the pulsar-wind Lorentz factor

As alluded in Sect. 1, approximating the pulsar wind by a non-relativistic flow can underestimate the pulsar-to-star wind energy-flux ratio, for a given momentum-flux ratio, by a factor of $v/2c$. This can be (roughly) solved assuming a mildly relativistic pulsar-wind velocity while keeping the Newtonian treatment, which leads to moderately unphysical results. However, there are additional, more fundamental, differences between relativistic and Newtonian flows that are relevant to the problem considered here. In this section, we discuss the impact of adopting a relativistic model for the simulated flows, and the influence of the specific value of the pulsar-wind Lorentz factor. For instance, although the results obtained in the mildly and highly relativistic cases are similar, the KH instability will tend to develop faster in the former. The impact of a non-relativistic approximation for the simulated flows is however stronger, since the shocked flow dynamics will be substantially different when orbital motion is included, even for the mildly relativistic case adopted in Sect. 2.

3.1. The colliding wind region at $\Gamma = 10$

We simulated the central part of the interaction region assuming a pulsar wind with $\Gamma = 10$ instead of 2. The geometry and system properties were the same as in Sect. 2, including orbital motion, and $\eta = 0.3$. The simulation was run long enough to reach a quasi-steady state on the considered scales of both $x \in [0, 4a]$ and $y \in [0, 4a]$, with the optical star located at $(2a, 2a)$. The adopted value of the wind Lorentz factor required an effective resolution of the computational grid of about three times the one adopted in Sect. 2, now with a domain size of 768×768 cells. The resulting maps for the distribution of density, temperature, and the spatial component of the four-velocity are shown in Figs. 7, 8, and 9. The plot shown in the bottom panel of Fig. 7 illustrates that the CD can change strongly on

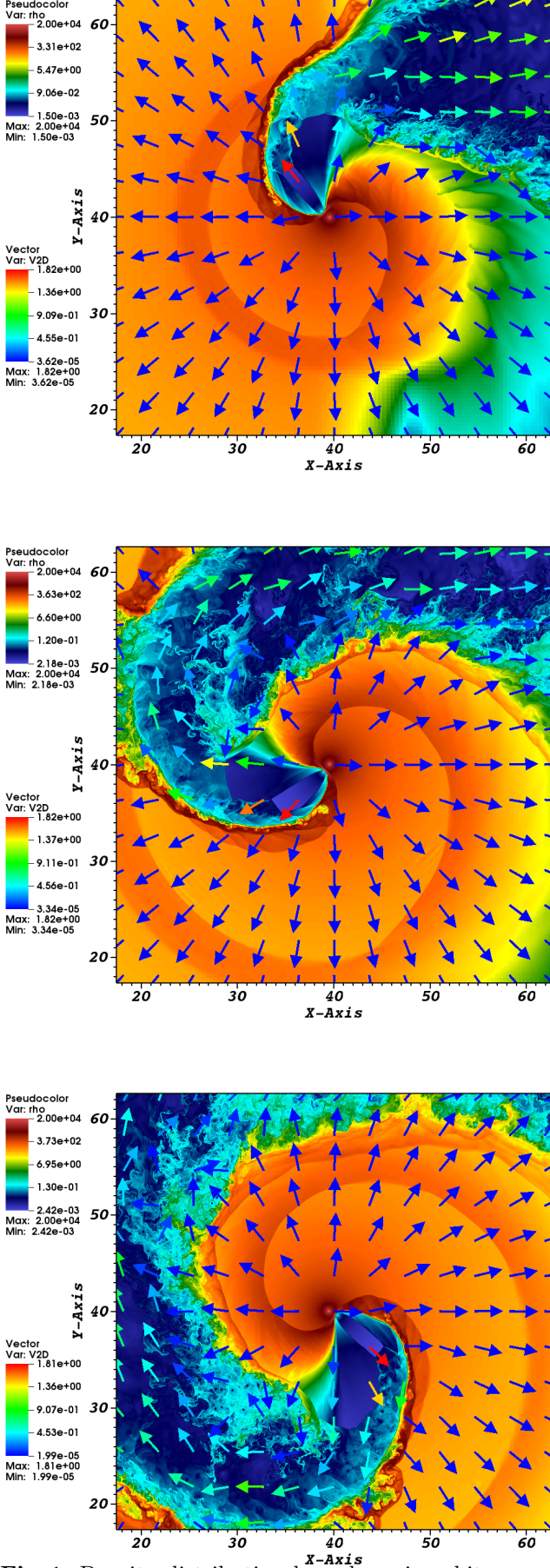


Fig. 1. Density distribution by colour, in arbitrary units, at times $t = 1.2 \times 10^5$ (top), 2.1×10^5 (middle) and 2.7×10^5 s (bottom), for the case with $\eta = 0.3$. The colored arrows show the four-velocity space component for different locations, and the axes units are a , which applies to all figures.

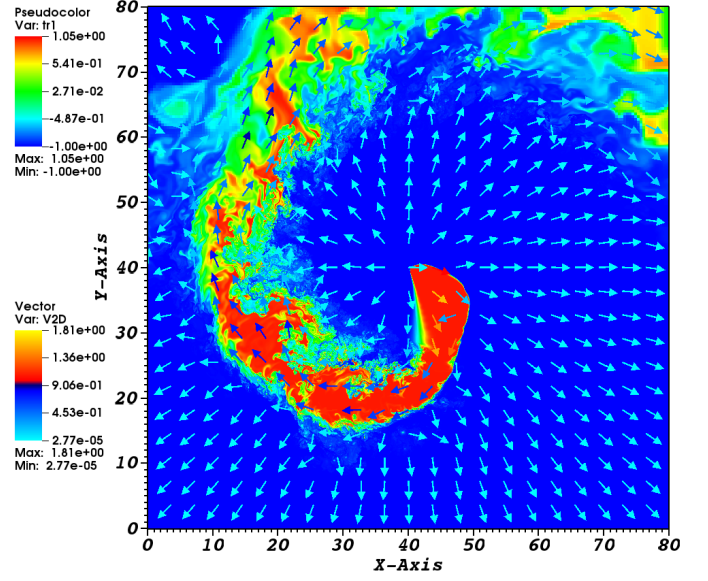


Fig. 2. Tracer distribution by colour, where 1 is only pulsar wind and -1 only stellar wind, at $t = 2.7 \times 10^5$ s, for the case $\eta = 0.3$.

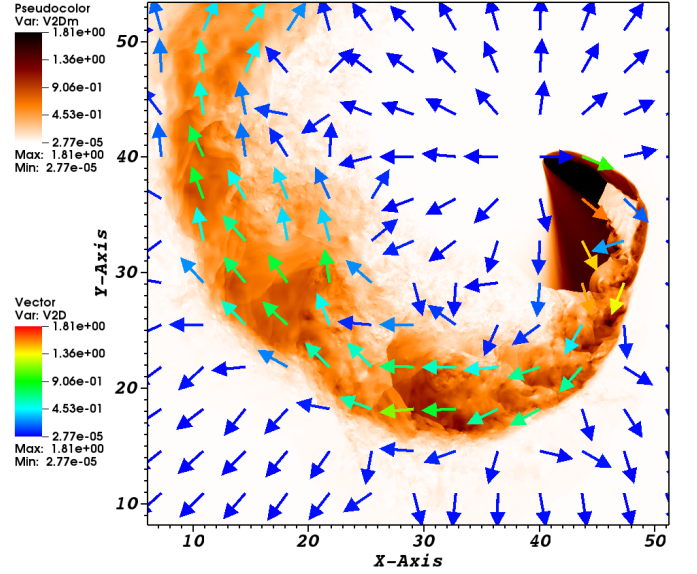


Fig. 3. Distribution by colour of the module of the spatial component of the four-velocity at $t = 2.7 \times 10^5$ s, for the case $\eta = 0.3$.

timescales much shorter than the binary period. The results of this numerical test show that strong shocks induced by the orbital motion are still present when the pulsar-wind Lorentz factor is higher, and the reacceleration of the shocked pulsar wind is stronger in the case of $\Gamma = 10$ than for $\Gamma = 2$. As shown in Sect. 3.3, the shocks induced by the orbital motion are a general feature when adopting a relativistic flow model, and they should also be present in the ultra-relativistic case. Regarding the development of the KH instability at the CD, in the considered case the growth rate does not seem to be significantly reduced. However, this conclusion may not be generalized in a straightforward

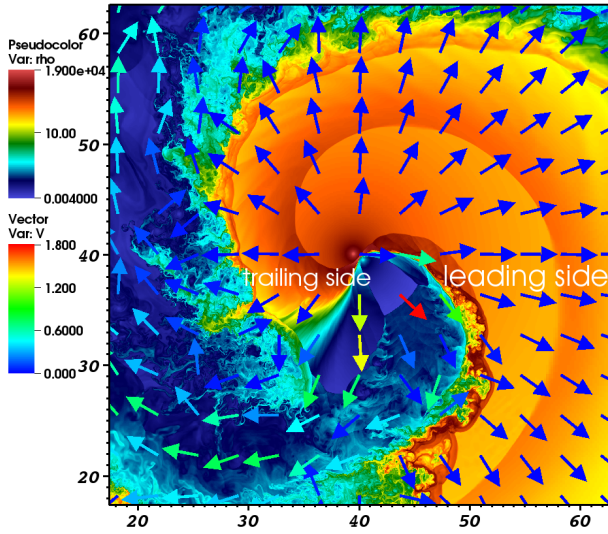
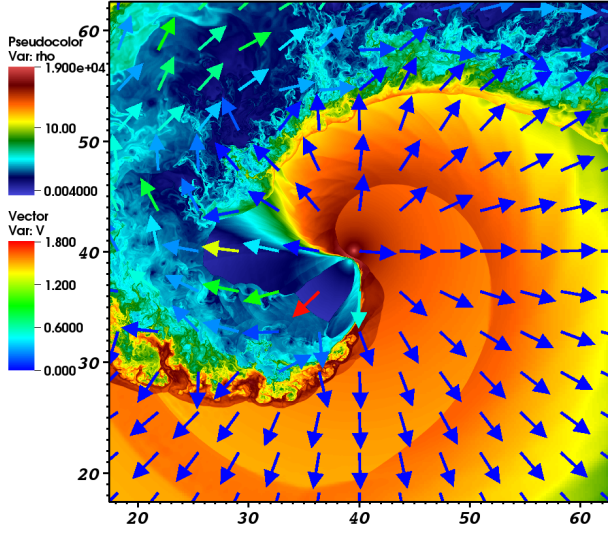
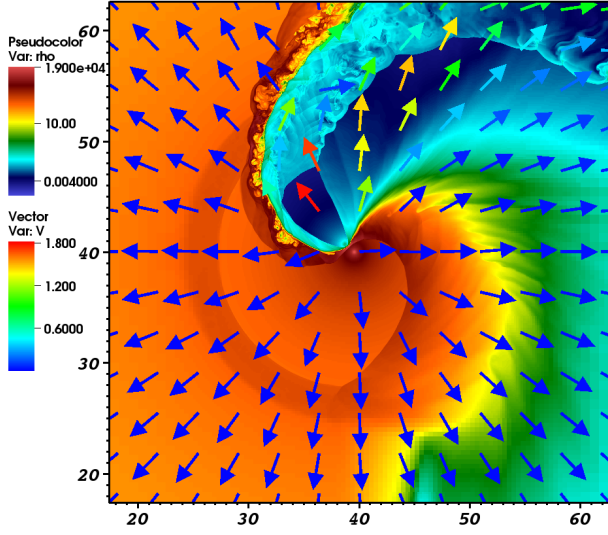


Fig. 4. The same as in Fig. 1 but for the case $\eta = 0.6$. The trailing and the leading sides of the interaction structure are indicated at the bottom panel.

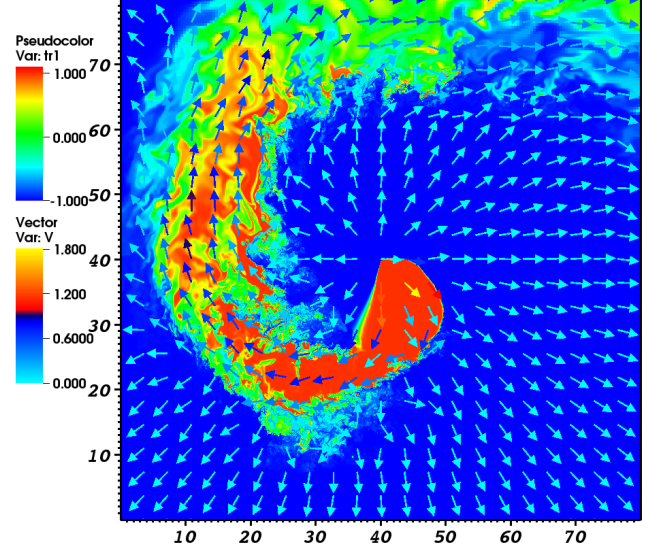


Fig. 5. The same as in Fig. 2 but for the case $\eta = 0.6$.

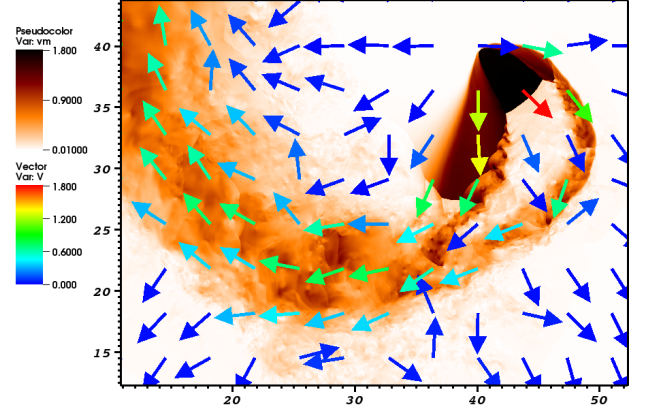


Fig. 6. The same as in Fig. 3 but for the case $\eta = 0.6$.

way to the ultra-relativistic case, which is considered in the next section.

3.2. Instability growth at the CD and Γ

Although the shocked structure evolution is the result of the interplay of different mechanisms operating on different scales, the KH instability developing in the CD can by itself have a strong impact on the flow structure. To study the instability growth in the CD, we performed 2D test simulations of the shocked pulsar and stellar winds adopting a mildly and an ultra-relativistic pulsar wind. The context of the simulations is the scenario described in Sect. 2. The calculations were performed with a relativistic hydrodynamical code whose characteristics are described for instance at the end of Sect. 2 in Perucho et al. (2005). The size of the computational box was $10^{12} \text{ cm} \times 3.3 \cdot 10^{11} \text{ cm}$, and the resolution, 1920×640 cells. The two shocked winds are homogeneous in the direction perpendicular to the simulated plane, and are initially in thermal pressure balance. It was assumed that the shocked pulsar wind had already been reaccelerated, thus the thermal pressure was significantly

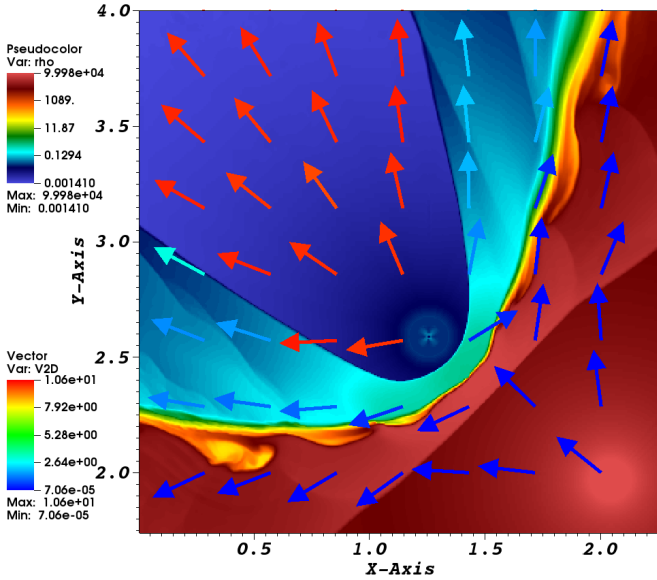
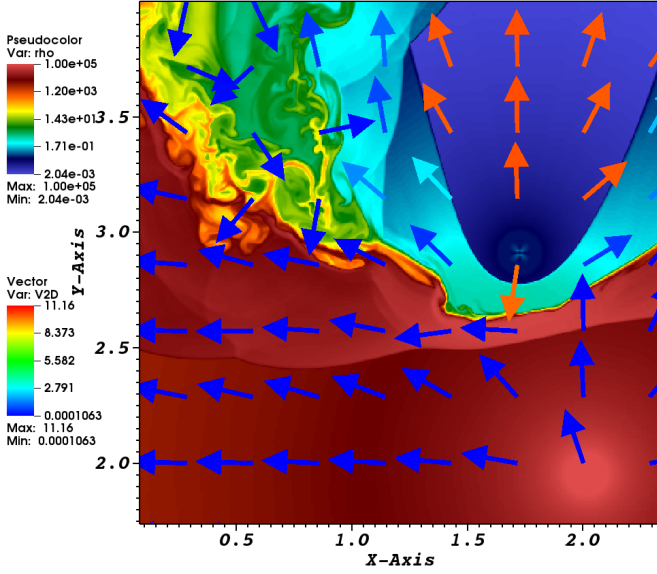


Fig. 7. Top: Density distribution by colour of the interaction region for a pulsar wind with $\Gamma = 10$ and $\eta = 0.3$. The domain shown is limited to highlight the interaction region. Bottom: The same as in the top but few hours later, to illustrate that the CD can change strongly on timescales much shorter than the binary period.

lower than the ram pressure. The shocked stellar wind was located at the upper half of the computational box (see below) and was assumed to be initially at rest.

The results for the density distribution illustrating the growth of seed perturbations are presented in Figs. 10 and 11. The pulsar wind in Fig. 10 has a bulk Lorentz factor of 2, and a thermal pressure of about 10% of the ram pressure. In Figure 11, the pulsar-wind bulk Lorentz factor is 10, and the microscopic Lorentz factor in the flow frame, related to temperature, is 10^5 . This case is very different from the case considered in Sect. 3.1, and would roughly correspond to a shocked and reaccelerated ultra-relativistic wind with (un-

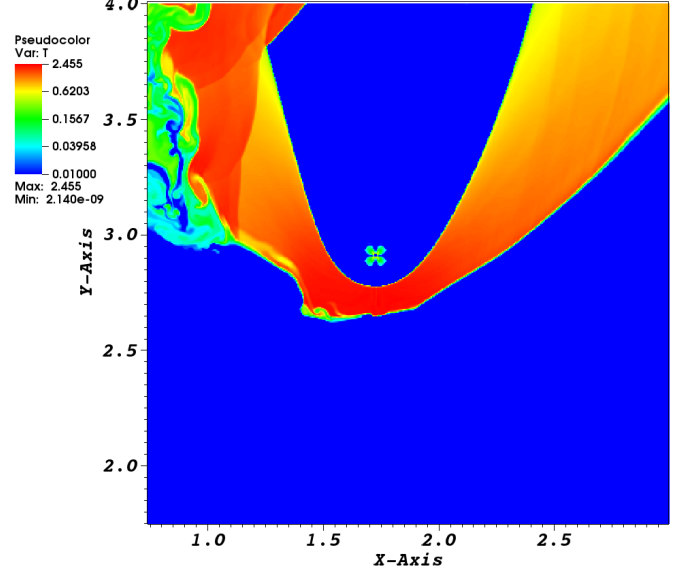


Fig. 8. The same as in Fig. 7 but for the temperature.

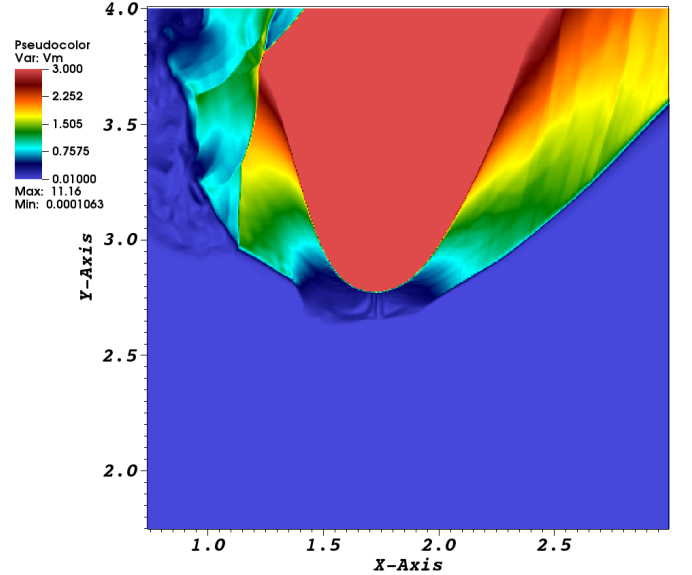


Fig. 9. The same as in Fig. 7 but for the module of the spatial component of the four-velocity.

shocked) $\Gamma \sim 10^6$. A comparison of Figs. 10 and 11 shows that, in the ultra-relativistic case, the development of the KH instability is significantly weaker, which is consistent with earlier numerical studies. In particular, a discussion of the reduction in the instability growth and related non-linear effects (namely mixing, disruption, and deceleration) for high Lorentz-factor flows can be found in Perucho et al. (2004a), Perucho et al. (2004b), and Perucho et al. (2005), in the context of planar and axisymmetric cylindrical jets.

Although the situation considered in this study has been very much simplified, one may still draw the conclusion that the shocked structure in high-mass binaries hosting a pulsar is less likely to develop the KH instability than massive star binaries. However, even in the case of an ultra-relativistic flow, the figures show that there is still a significant growth

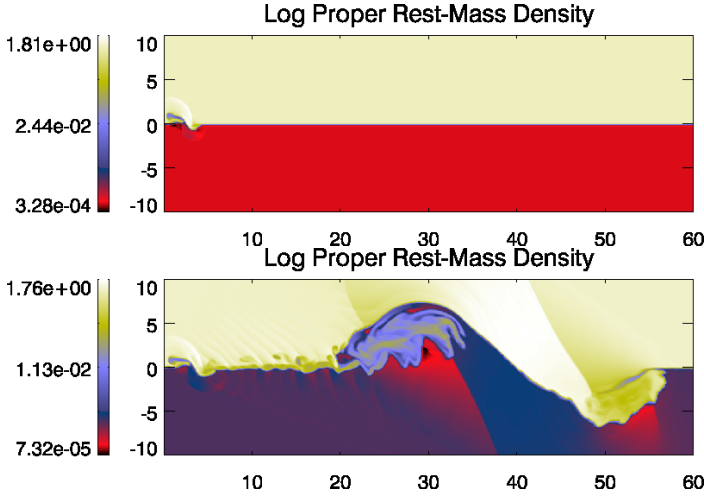


Fig. 10. Density distribution by colour in arbitrary units of the development of instabilities at the contact discontinuity after 2.8 (top) and 43 s (bottom) from the beginning of the simulation, for a mildly relativistic pulsar wind. The axes units are 1.7×10^{10} cm.

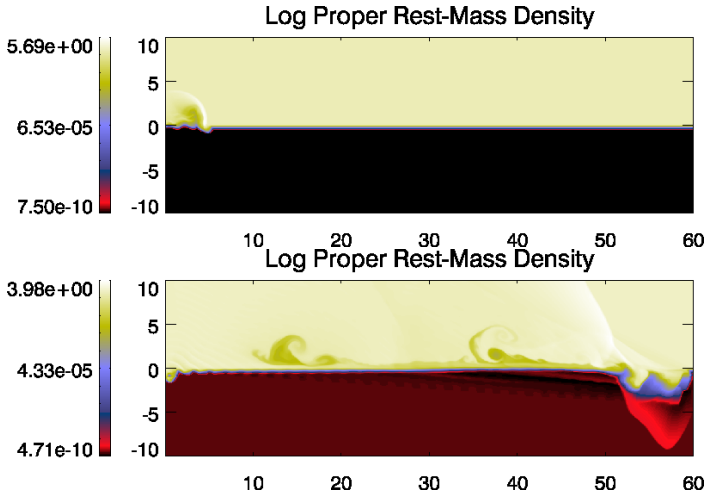


Fig. 11. The same as in Fig. 10 but after 2.8 (top) and 34 s (bottom), for the case with a bulk Lorentz factor of the shocked pulsar wind of 10 (in the laboratory frame), and a microscopic Lorentz factor for the particles of 10^5 (in the flow frame).

of the KH instability on scales comparable to those of the binary system. This, plus the strong asymmetry of the interaction introduced by orbital motion, makes the generation of shocks and turbulent flows at the CD very likely on scales of $\sim a$, regardless of the value of Γ .

3.3. Relativistic vs Newtonian inertia

Orbital motion introduces a strong non-stationary component in the dynamics of the shocked structure. In such a case, the inertia of the flow has a very strong influence, and there is a major difference between the relativistic and Newtonian case: the relativistic inertia is proportional to pressure when this is not negligible compared to the rest mass energy (as expected here), whereas Newtonian inertia is proportional to density. Therefore, although Newtonian simulations may reproduce the geometry of the interaction

region within the system, where the orbital motion is negligible, on scales $\gtrsim a$ the Coriolis force starts to deflect the flow, and inertia then becomes important.

If one of the shocked winds is at least mildly relativistic, for it to be significantly deflected the exerted lateral pressure is to be a substantial fraction of the ram pressure of the flow. Since the plasma flowing out from the system is already trans-sonic, this lateral pressure will be $(\Gamma^2 \times)$ higher than the thermal pressure, and the flow deflection will produce shocks. These shocks, which are stronger for higher Γ , will trigger large CD perturbations, and can be a source of energy dissipation in the form of particle acceleration.

In a Newtonian flow with the momentum and energy fluxes of the shocked pulsar wind, density and therefore inertia would be very small even if the plasma were relatively hot. Such a fluid could be smoothly deflected by sound waves, rendering a much more stable structure without much non-thermal activity. This conclusion also applies if the wind has a non-relativistic velocity but the same momentum flux, and thus smaller energy flux, than its relativistic counterpart.

The effects discussed here balance the higher stability of the CD with an ultra-relativistic pulsar wind discussed in Sect. 3.2. By itself, the instability growth rate would depend on (small) seed perturbations of the CD of some sort. However, under orbital motion, strong non-linear perturbations are unavoidable, as shown in Sect. 3.1. We note that this conclusion is based on the relativistic nature of the flow, and does not apply to massive star binaries with colliding winds.

4. Discussion

The simulation results show that the colliding pulsar and stellar winds produce a coherent flow with low entropy up to only a few a . Beyond that point, for stellar and pulsar winds typical for gamma-ray binaries (possibly) hosting a non-accreting pulsar, the shocked flow becomes bent, non-ballistic, and highly turbulent, with strong wind mixing. It seems therefore unlikely that the shocked structure will remain as a spiral on scales $\gg a$ (even for $\eta = 0.6 \lesssim 1$). As seen by comparing the cases with $\eta = 0.3$ and 0.6 , the smaller the two-wind momentum flux ratio, the earlier the shocked structure is closed and disrupted by the orbital motion. Overall, the flow evolution is quite similar to earlier analytical predictions (Bosch-Ramon & Barkov 2011).

The adopted Γ -value already captures the main physics of the colliding wind region and the shocked structure formed there. Higher wind Lorentz factors may yield more stable flows at the CD in an idealized situation, but the impact of orbital motion enhances instability and triggers shocks, and overall the global picture should not change dramatically between $\Gamma = 2$ and $\Gamma \gg 1$. Newtonian simulations thus seem suitable only for the colliding wind region on its smallest scales, within the binary, because further out the impact of orbital motion will be much smoother than in the relativistic case, missing much of the instability and shock generation. In addition, a non-relativistic pulsar wind, unlike its relativistic counterpart, could not re-accelerate and its speed could not then again approach c after being shocked.

In addition to the pulsar-wind shock facing the star, and the unshocked pulsar wind itself, the present calculations reveal additional sites of non-thermal activity (as

hinted already in Bosch-Ramon & Barkov 2011). Most of the pulsar-wind kinetic energy that is not reprocessed on the binary system scales is converted into internal energy farther out, either through strong shocks in the direction away from the star, or through weaker shocks and turbulence further downstream. Given their proximity to the binary system, the strong shocks *behind* the pulsar seem ideal sites for particle acceleration and high-energy emission. For instance, farther from the binary, the expected weaker synchrotron and inverse Compton losses would allow the accelerated particles to reach higher energies. This could explain the very energetic photons seen from LS 5039 (Khangulyan et al. 2008a). In addition, an emitter farther from the star would allow gamma rays to avoid severe absorption in the stellar photon field (e.g., Bosch-Ramon et al. 2008). Finally, the presence of emitting regions with different physical conditions may explain the broad-band spectrum in some gamma-ray binaries (e.g. Takahashi et al. 2009; Zabalza et al., in preparation).

The complex hydrodynamics of the shocked flow on scales $\gg a$, with weak shocks and turbulence, indicates that radio-emitting electrons may be accelerated there instead of at the termination shock facing the star, where free-free radio absorption can be severe, and the high energies of the accelerated electrons (e.g., Kennel & Coroniti 1984) are unsuitable for efficient radio emission. The radio electrons will initially move at mildly relativistic speeds, at least in most of the emitting flow, but for $r \gtrsim 100a$ further mixing will likely slow down the flow. The spatial scale of the simulated flow corresponds to $\sim 10 - 100$ millarcseconds at ~ 2 kpc distance, so the production and evolution of the radio-emitting electrons, and the structure of the underlying flow, can be studied with current VLBI instrumentation (see Dhawan et al. 2006; Ribó et al. 2008; Moldón et al. 2011a,b).

The mildly relativistic speeds downstream of the strong shocks in the pulsar wind imply that Doppler boosting can be significant there (as proposed in Khangulyan et al. 2008b; see also, e.g., Dubus et al. 2010). However, we must emphasize that the motion of the whole interaction structure is non-ballistic, with rather complex velocity distributions both in terms of module and direction. This should induce through Doppler boosting complicated variability patterns with different timescales in the non-thermal emission. This variability would appear on top of that intrinsic to the non-thermal activity itself.

Acknowledgements. We thank an anonymous referee for useful and constructive suggestions. The calculations were carried out in the cluster of Moscow State University *Chebyshev*. We thank Andrea Mignone and the *PLUTO* team for the possibility to use the *PLUTO* code. We also thank the *Chombo* team for the possibility to use the *Chombo* code. The visualization of the results was done using the VisIt package. The research leading to these results has received funding from the European Union Seventh Framework Program (FP7/2007-2013) under grant agreement PIEF-GA-2009-252463. V.B.-R. acknowledges support by the Spanish *Ministerio de Ciencia e Innovación* (MICINN) under grants AYA2010-21782-C03-01 and FPA2010-22056-C06-02, and MP acknowledges support by the Spanish *Ministerio de Ciencia e Innovación* (MICINN) grants AYA2010-21322-C03-01, AYA2010-21097-C03-01 and CONSOLIDER2007-00050.

References

Abdo, A. A., Ackermann, M., Ajello, M., et al. 2011, ApJ, 736, L11
 Abramowski, A., Acero, F., Aharonian, F., et al. 2012, A&A, 541, A5
 Ackermann, M., Ajello, M., Ballet, J., et al. 2012, Science, 335, 189

Aharonian, F., Akhperjanian, A. G., Aye, K.-M., et al. 2005, A&A, 442, 1
 Aharonian, F. A., Bogovalov, S. V., & Khangulyan, D. 2012, Nature, 482, 507
 Ball, L. & Kirk, J. G. 2000, Astroparticle Physics, 12, 335
 Barkov, M. V. & Khangulyan, D. V. 2012, MNRAS, 2375
 Bednarek, W. 2011, MNRAS, 418, L49
 Blondin, J. M. 1994, ApJ, 435, 756
 Blondin, J. M., Stevens, I. R., & Kallman, T. R. 1991, ApJ, 371, 684
 Bogovalov, S. V., Khangulyan, D., Koldoba, A. V., Ustyugova, G. V., & Aharonian, F. A. 2012, MNRAS, 419, 3426
 Bogovalov, S. V., Khangulyan, D. V., Koldoba, A. V., Ustyugova, G. V., & Aharonian, F. A. 2008, MNRAS, 387, 63
 Bongiorno, S. D., Falcone, A. D., Stroh, M., et al. 2011, ApJ, 737, L11
 Bosch-Ramon, V. & Barkov, M. V. 2011, A&A, 535, A20
 Bosch-Ramon, V. & Khangulyan, D. 2009, International Journal of Modern Physics D, 18, 347
 Bosch-Ramon, V., Khangulyan, D., & Aharonian, F. A. 2008, A&A, 489, L21
 Chernyakova, M., Neronov, A., & Walter, R. 2006, MNRAS, 372, 1585
 Colella, P., Graves, D. T., Keen, N. D., et al. 2009, Library, 42
 Colella, P. & Woodward, P. R. 1984, Journal of Computational Physics, 54, 174
 Dhawan, V., Mioduszewski, A., & Rupen, M. 2006, in VI Microquasar Workshop: Microquasars and Beyond
 Dubus, G. 2006, A&A, 456, 801
 Dubus, G., Cerutti, B., & Henri, G. 2010, A&A, 516, A18
 Gayley, K. G., Owocki, S. P., & Cranmer, S. R. 1997, ApJ, 475, 786
 Johnston, S., Manchester, R. N., Lyne, A. G., et al. 1992, ApJ, 387, L37
 Johnston, S., Manchester, R. N., McConnell, D., & Campbell-Wilson, D. 1999, MNRAS, 302, 277
 Kennel, C. F. & Coroniti, F. V. 1984, ApJ, 283, 710
 Khangulyan, D., Aharonian, F., & Bosch-Ramon, V. 2008a, MNRAS, 383, 467
 Khangulyan, D., Aharonian, F. A., Bogovalov, S. V., & Ribó, M. 2011, ApJ, 742, 98
 Khangulyan, D., Aharonian, F. A., Bogovalov, S. V., & Ribo, M. 2012, ApJ, in press
 Khangulyan, D., Hnatic, S., Aharonian, F., & Bogovalov, S. 2007, MNRAS, 380, 320
 Khangulyan, D. V., Aharonian, F. A., Bogovalov, S. V., Koldoba, A. V., & Ustyugova, G. V. 2008b, International Journal of Modern Physics D, 17, 1909
 Lamberts, A., Dubus, G., Lesur, G., & Fromang, S. 2012, A&A, submitted [astro-ph/1202.2060]
 Mignone, A. & Bodo, G. 2005, MNRAS, 364, 126
 Mignone, A., Bodo, G., Massaglia, S., et al. 2007, ApJS, 170, 228
 Moldón, J., Johnston, S., Ribó, M., Paredes, J. M., & Deller, A. T. 2011a, ApJ, 732, L10
 Moldón, J., Ribó, M., & Paredes, J. M. 2011b, A&A, 533, L7
 Negueruela, I., Ribó, M., Herrero, A., et al. 2011, ApJ, 732, L11
 Okazaki, A. T., Nagataki, S., Naito, T., et al. 2011, PASJ, 63, 893
 Perucho, M., Hanasz, M., Martí, J. M., & Sol, H. 2004a, A&A, 427, 415
 Perucho, M., Martí, J. M., & Hanasz, M. 2004b, A&A, 427, 431
 Perucho, M., Martí, J. M., & Hanasz, M. 2005, A&A, 443, 863
 Pittard, J. M. 2009, MNRAS, 396, 1743
 Ribó, M., Paredes, J. M., Moldón, J., Martí, J., & Massi, M. 2008, A&A, 481, 17
 Romero, G. E., Okazaki, A. T., Orellana, M., & Owocki, S. P. 2007, A&A, 474, 15
 Takahashi, T., Kishishita, T., Uchiyama, Y., et al. 2009, ApJ, 697, 592
 Tam, P. H. T., Huang, R. H. H., Takata, J., et al. 2011, ApJ, 736, L10
 Tavani, M. & Arons, J. 1997, ApJ, 477, 439
 Torres, D. F. 2011, in High-Energy Emission from Pulsars and their Systems, ed. D. F. Torres & N. Rea, 531